Journal of Materials Chemistry A

ROYAL SOCIETY OF CHEMISTRY

PAPER

View Article Online
View Journal

Cite this: DOI: 10.1039/d5ta09847e

High cyclic reversibility in eutectic lithium calcium anodes characterised by electron microscopy

Ed Darnbrough, * Sreejith Olakkil Veedu, Zhuojun Hou, Myra Ng, Jack Aspinall, Chris Grovenor, Peter D. Nellist and David E. J. Armstrong

Lithium metal is the benchmark anode for lithium-ion battery technology with high theoretical energy density and capacity. However, dendrite formation and solid electrolyte interphase formation limit the practical current density and lifetime, respectively. This study investigates how a lithium–calcium alloy can overcome these challenges by fabricating a simple to manufacture anode made of two phases in a 3D structure. Exploration with different electrolytes and electron microscopy highlights the role the calcium intermetallic plays in lithium cycling. The charge transfer resistance of electrolytes is 255 Ohms for LiTFSI and 315 Ohms for LiPF6. The overpotential value of both electrolytes within a symmetric eutectic anode cell is 0.06 V for LiTFSI compared to 0.26 V for LiPF6, highlighting that the electrolyte can alter the deposition mechanism not just the total cell resistance. We conclude that both the current density and long term cycling performance are improved *versus* lithium metal anodes, as the 3D Li–Ca matrix can suppress volume changes during cycling and remove the need for lithium metal to be present at the interface with the electrolyte, thereby reducing side reactions.

Received 2nd December 2025
Accepted 19th April 2026

DOI: 10.1039/d5ta09847e

rsc.li/materials-a

1 Introduction

Lithium-ion batteries are widely used in portable electronics and are now rapidly establishing a dominance in automobiles as well as the potential to power electric flight.[1] However, this demands improvements in efficiency, energy density and safety over the current designs. Typical lithium-ion batteries use intercalation anodes like graphite because of the reactivity of lithium metal with standard electrolytes, but a theoretical increase in capacity could be realised by moving to a metallic anode (3860 mA h g^{-1} *versus* 372 mA h g^{-1}).[2] Lithium metal alone as an anode has shown problems like low coulombic efficiency and poor cycle life.[3] This is hypothesized to be a result of uneven lithium plating during charging and dendrite growth that lead to 'dead lithium' reducing capacity or short circuits causing cell failure.[4,5] Attempts to reduce dendrite formation have used additional 3D porous structures to make composite anodes, but these face challenges of low lithiophilicity resulting in electrodes that are not fully dense.[6–8] Alloying lithium to produce anodes with self-assembled eutectic microstructures instead of a pre-manufactured 3D structure has the potential to achieve the current densities and charging rates required for EV application.[9] Jia *et al.* showed that these eutectic anodes can suppress lithium dendrite growth by favouring uniform deposition during plating. However, understanding how these new materials function as anodes requires characterisation of detailed mechanisms of how lithium is stripped from or plated on a eutectic microstructure, using microscopy and spectroscopy.[10] This work investigates the material properties and mechanisms behind the reduced capacity loss achieved in eutectic anode batteries. This is achieved by producing a self-assembling anode from a two-phase material; pure lithium metal, to be cycled, and a lithium intermetallic that remains as a three-dimensional scaffold to provide both electrical and ionic contact between the current collector and the electrolyte throughout cycling. Further development of these alloys requires a full understanding of the mobility of lithium through these distinct phases and the microstructures produced by manufacturing, and how these change with cycling. The choice of alloying material is important for device engineering (minimising any loss in energy density and side reactions) and economically (cheap, abundant, and anodes that are easy to prepare).

Alkali earth metals (Ca, Sr, Ba, *etc.*) all have low temperature eutectic reactions in their equilibrium phase diagram between an intermetallic and lithium metal. This reaction allows for easy production of thin anodes *via* solidification onto a current collector, resulting in flat, thin anodes (<100 μm) with a 3D microstructure of the two phases that is tuneable by the composition of the melt.[11] Importantly, for application as an anode, the intermetallic phases are both electrically and ionically conducting[12,13] but are not physically removed like the lithium metal during battery discharge (stripping at the anode). Wang *et al.*[14] showed that the Li–Ca alloy could be used to increase the lithiophilicity of carbon cloth as an adaptation of a standard graphite intercalation anode. They report that this 330 μm thick structure is capable of a long cycling lifespan of 1100 h in a liquid electrolyte

Materials Department, University of Oxford, Oxford, UK. E-mail: ed.darnbrough@materials.ox.ac.uk

(LiTFSI) symmetric cell with a current density of 5 mA cm^{-2} and maintains a fixed areal capacity of 5 mA h cm^{-2}. Jia *et al.*[9] fabricated Li–Ca alloys containing 2, 9 and 17 at% calcium, and on cycling using a LiTFSI liquid electrolyte they showed that the Li–9 at%Ca alloy (∼ eutectic composition) had the highest cycle life at a current density of 1 mA cm^{-2} and was stable for up to 500 cycles. The morphology of the Li–9 at%Ca alloy anode surface after cycling was smooth and compact, suggesting that Li plating occurred uniformly. Jia *et al.* recognised that with simple scanning electron imaging they were unable to 'reveal the boundary' between the deposited Li and the starting electrode, and so assume this demonstrates uniform plating but that the precise details require further investigation. Additionally, the anodes investigated by Jia *et al.* involved very thick electrodes on the order of ∼200 μm, and the impact of reducing the anode thickness to that required for a commercial battery needs a greater understanding of the mechanisms of lithium movement during cycling. Herein, we used different electrolytes (to alter the lithium nucleation potential and side reactions) and investigated using electron microscopy where lithium plating occurred in the eutectic structure and explored if the lithium during cycling re-entered the bulk anode and not just caused plating onto the surface above the intermetallic structure. The electrolytes chosen were LiTFSI and $LiPF_6$ as they are common lithium metal anode electrolytes that have been shown to have differing effects on lithium plating morphologies, which is an indication of different nucleation *vs.* growth potentials.[15]

2 Results and discussion

2.1 Phase identification

The microstructure of the cast eutectic depends on the composition of the starting melt, with the volume fraction of the intermetallic scaffold phase reducing with reduced calcium concentration, Fig. 1. In these secondary electron scanning electron microscopy (SEM) images, the pure lithium phase is dark and the Li_2Ca intermetallic is grey. When the liquid composition is lithium poor (79 at%/40 wt% Li), the microstructure is dominated by the intermetallic phase grown in a dendritic morphology, with only small amounts of lithium metal visible (Fig. 1a). At the other extreme, the alloy with 98 at% (90 wt%) Li provides a microstructure with large lithium metal regions surrounded by bands of the eutectic of alternating lithium metal and intermetallic (Fig. 1d). This lithium-rich eutectic microstructure (LREM) was selected for anode production to provide the maximum cyclable capacity while retaining enough intermetallic to act as a scaffold. Energy dispersive X-ray (EDX) spectroscopy with SEM confirms the cast material has two distinct phases, one containing the calcium and one without (Fig. S1). Standard EDX spectroscopy cannot detect lithium, so transmission electron microscopy (TEM) diffraction analysis from lamella extracted by plasma focused ion beam (PFIB) lithography was used to show that the two phases in the anode material match with two distinct crystallographic phases, body centred cubic lithium metal with the space group $Im\bar{3}m$ and hexagonal crystal Li_2Ca with the space group $P63/mmc$ (Fig. 2).[9,11] In this figure, the contrast of the two phases is reversed compared to the SEM images, because in the TEM image bright regions correspond to high transmission of electrons (lithium metal) and dark regions indicate diffraction or absorption of electrons.[16]

2.2 Galvanostatic cycling

2.2.1 Comparison of electrolytes. The choice of electrolyte in lithium metal cells has been found to cause distinct changes in the voltage profile by altering the formation and nature of the solid electrolyte interphase (SEI) and the kinetics of lithium dendrite nucleation.[17] Wood *et al.* showed that a half-cycle voltage potential

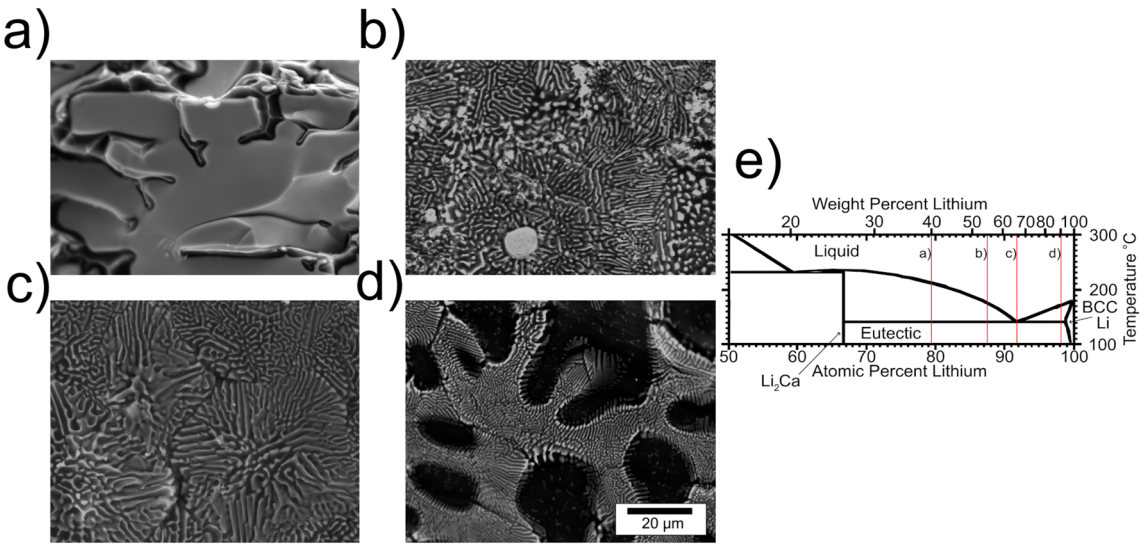

Fig. 1 Secondary electron SEM images showing the surface with different compositions of the Li–Ca eutectic system: (a) 79 at%/40 wt% Li, (b) 87 at%/55 wt% Li, (c) 92 at%/66 wt% Li, and (d) 98 at%/90 wt% Li. In each micrograph, the lithium metal phase has the darkest contrast and the lithium calcium intermetallic has a lighter grey contrast, and the magnification is the same for all images. (e) A section of the equilibrium Li–Ca phase diagram adapted from ref. 9, where each colour denotes a different phase, and regions with two colours are compositions where two phases are expected.

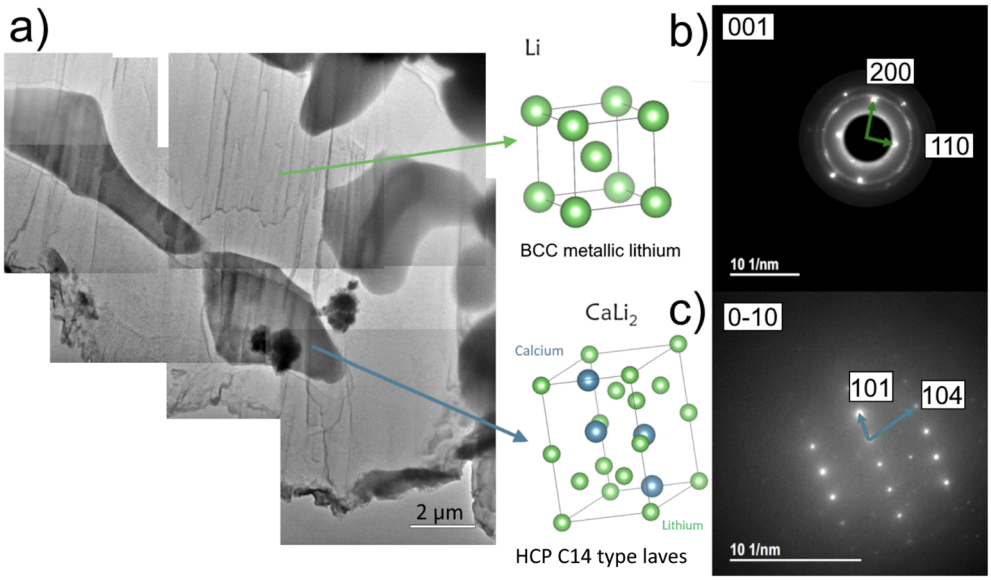

Fig. 2 (a) A composite TEM image showing the as-cast eutectic structure. (b and c) Diffraction patterns and the crystal structure of the two phases found in the eutectic with the beam direction given in the top left. The rings in the lithium metal diffraction pattern match LiO_2 from a surface oxide layer on the TEM lamella. The vertical lines in the image are a curtaining (topological) effect due to the process of PFIB production of the TEM foil, but the final step low kV polishing means there is no observable damage to the microstructure or crystal structure.

can be interpreted as a sum of the potential contributed from both the anode and cathode electrodes (assuming during cycling an unchanging contribution directly from the electrolyte). In this case, the initial voltage of the half-cycle is dominated by a contribution from the cathode (deposition nucleation) and the latter by the anode (stripping from the bulk). It is proposed that when the kinetics of the anode and cathode are balanced there should be a minimum in cell over-potential. In this work, comparison between lithium metal electrodes and LREM anodes has been made in two electrolytes (LiTFSI and $LiPF_6$). It has been reported in the lithium metal system that cells with $LiPF_6$ produce a higher potential during each half-cycle than an otherwise equivalent cell using LiTFSI.[17] For the LREM symmetric cell, the same general trend is observed (Fig. 3a). The earlier and steeper secondary peak in the $LiPF_6$ cell can be interpreted using the Wood analogy to be the result of a depletion of easily available lithium sooner than in the LiTFSI cell (Fig. 3b). Analysing the position of this secondary peak after a higher number of cycles (or during a single long cycle) suggests that at least 30% of the plated capacity on each half-cycle in the $LiPF_6$ cell requires a greater potential which increases to

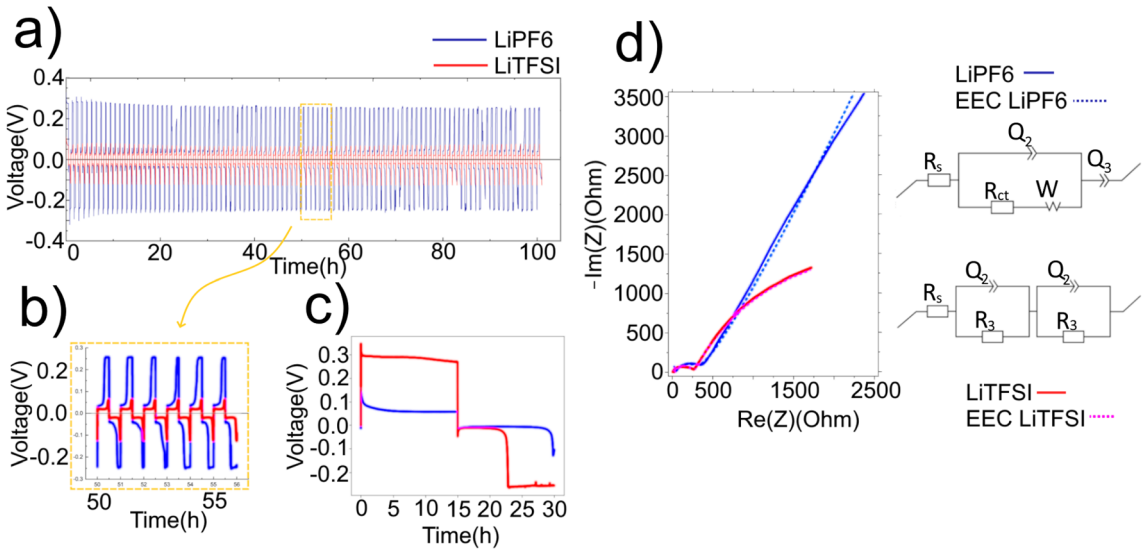

Fig. 3 Comparison of cycling of LREM symmetric cells with $LiPF_6$ (blue) and LiTFSI (red). (a) shows cycling at a current density of X mA cm^{-2} with 6 typical cycles highlighted in (b). (c) shows a single long cycle at a current density of Y mA cm^{-2}. (d) shows the EIS results taken before cycling, with their equivalent circuit models that produce the dashed lines.

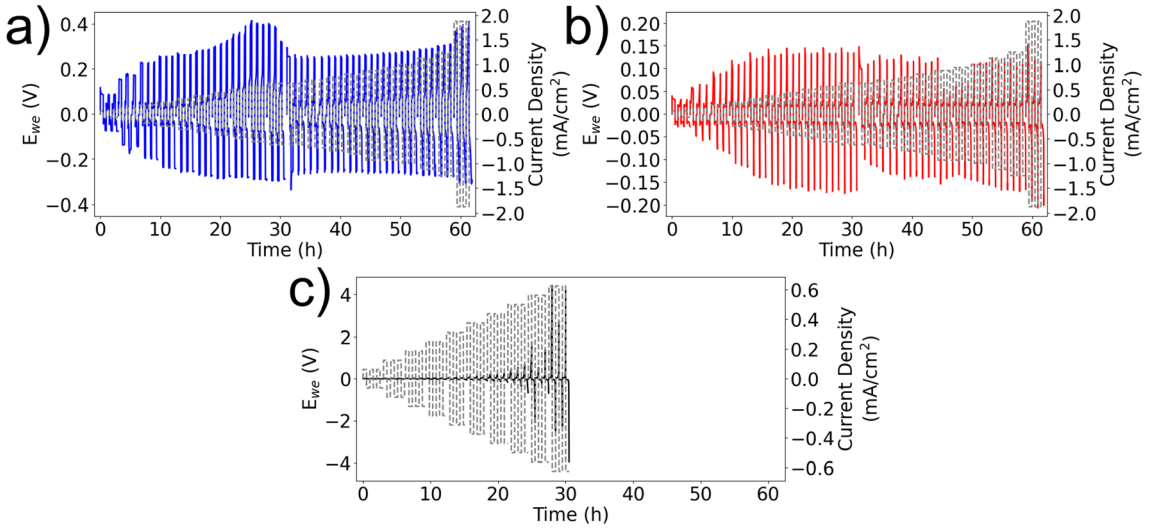

Fig. 4 Comparison of cell potential variations with stepped increases in current (dashed line) during cycling. (a and b) LREM symmetric cells with $LiPF_6$ and LiTFSI, respectively. (c) A lithium symmetric cell with LiTFSI. Note the different vertical axis scales. Fig. S2 is a version of this figure focusing on the first 25 h.

almost 50% when the half-cycle time is increased to 15 h (Fig. 3c). The constant potential in both electrolytes after the secondary peak is indicative of the voltage required to strip new lithium that is diffused from the bulk of the electrode. The fact that the potential is constant (or only a small decreases) after the lithium supply has changed, from the surface to the bulk, suggests that there is a stable source of lithium coming from the electrode bulk that is distinct from the shape observed in the lithium metal case, whereby pitting leads to an increase in the surface area of available lithium and so a measurable decrease in potential is observed.[17] This suggests that lithium in the latter part of the half-cycle is diffused from the bulk through the intermetallic, which provides a stable interface with the electrolyte. Electrochemical impedance spectroscopy (EIS) measurements show that the $LiPF_6$ solution resistance is greater than that for LiTFSI and that the $LiPF_6$ system is best modelled with a semi-infinite diffusion element, whereas the LiTFSI system can be fitted with a model containing two absorption capacitances (Fig. 3d). This suggests that there is a larger lithium ion diffusion gradient in the $LiPF_6$ system compared to the LiTFSI system, and this agrees with studies on pure lithium metal anodes where the SEI thickness and fraction of dead lithium are greater in contact with $LiPF_6$, producing a tortuous path for Li diffusion and the creation of a steeper gradient during cycling.[18]

Cycling the LREM electrodes with stepped increases in current produces a non-linear response in the maximum potential of each half-cycle, irrespective of the electrolyte (Fig. 4). Comparing with similar measurements on lithium metal symmetric cells, the cell potential of the initial peak (associated with nucleation at the cathode) and the limit reached after the second peak, representing stripping at the anode, show no increase once the current density is greater than 0.25 mA cm^{-2}. This suggests that the cell potential is controlled by a kinetic limit not the cell resistance.

Comparison between the two electrolytes with increasing half-cycle time illustrates that the position in the cycle where the potential increase appears is a function of the capacity plated on the previous half-cycle (Fig. 5a and c). Here, standard LREM symmetric cells were cycled at 0.125 mA cm^{-2} with an initial half-cycle time of 600 s (Fig. 5b(i)). To highlight the different electrodes, the measured potential during cycling has been plotted, where the purple color shows the stripping of one electrode and the inverted and shifted trace in green shows the stripping of the other electrode, to allow for easy comparison (Fig. 5a and c). Both cells show the expected high potential on the first half-cycle, indicative of the voltage required to extract lithium from the interior of the anode *via* diffusion through the intermetallic (0.04 V for LiTFSI and 0.25 V for $LiPF_6$), as shown in Fig. 5a(i) and c(i). The small initial peak in LiTFSI *vs.* $LiPF_6$ can be considered due to the difference in the nucleation potential on the smooth cathode interface. The maximum potential required for the second half-cycle stripping in both cases is higher than the initial stripping voltage from the pristine electrode, which may be indicative of a smaller effective area or a kinetic limit caused by any "dead" lithium or fresh SEI on the surface of the electrode. For the second set of cycling (ii), the half-cycle stripping from the initial electrode is increased to 1200 s, while the stripping time from the second electrode is held at 600 s, producing an asymmetry in the moved capacity during the cycling, as shown in Fig. 5b(ii). In the LiTFSI case, it removes the appearance of the secondary peak for the electrode stripped during the second half-cycle (green), but the peak for the first electrode stripped occurs after a similar amount of time to the plating time it experienced on the previous half-cycle, as shown in Fig. 5a(ii). As highlighted earlier, the profile after the peak is constant, suggesting a stable environment from which lithium is being stripped. After the asymmetric plating, one electrode will have accumulated for 1800 s of additional plating compared to the other electrode. When the cycle times are made

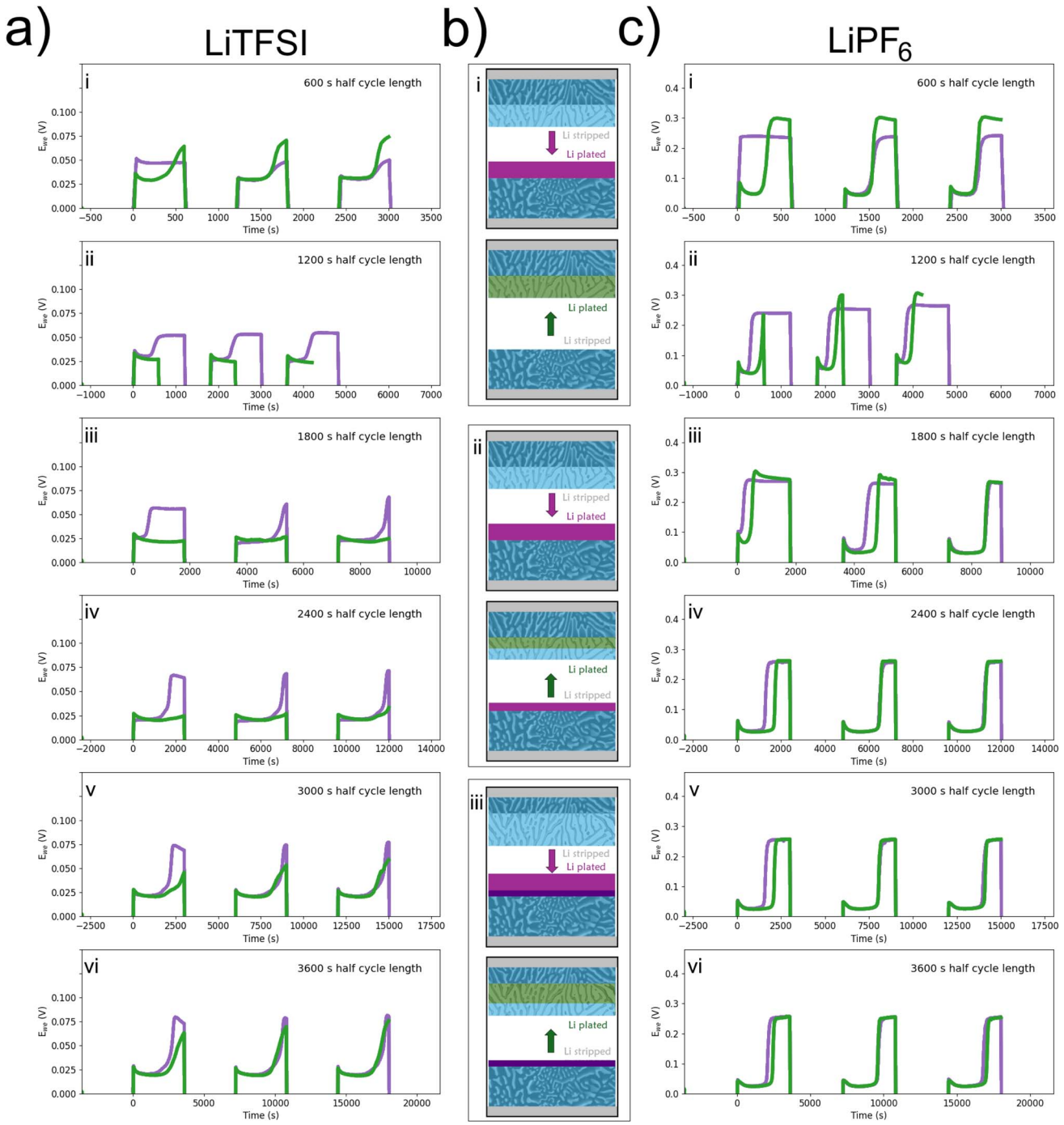

Fig. 5 Comparison of increasing half-cycle time in LREM symmetric cells in the two electrolytes. (a) LiTFSI and (c) $LiPF_6$ (note that the voltage scale for $LiPF_6$ is 4 times larger than that for LiTFSI). (b) Schematic of Li movement during half-cycles. Purple color indicates the response of the first half of each cycle and green color indicates the second half-cycle response inverted and shifted for easy comparison. For (a–c), (i) shows the Li movement during a 600 s half-cycle in both directions, (ii) shows the Li movement during a 1200 s first half-cycle and a 600 s second half-cycle, and (iii) shows the Li movement during a 1800 s half-cycle in both directions. (a & c) (iv–vi) are longer symmetric cycling with the same amount of lithium being moved in each direction.

symmetrical again, the asymmetry in the potential during a half-cycle, Fig. 5b(iii), continues until the half-cycles are extended to 3600 s, where both peak profiles are similar irrespective of which electrode is acting as the anode, Fig. 5a(iii) and (iv). In the $LiPF_6$ case, the asymmetrical cycling does not remove the secondary peak, and the potential profiles of each half-cycle are the same by the end of the set of 1800 s cycles even though the same capacity asymmetry should have been developed, Fig. 5c(iii and vi). Longer half-cycles show that the symmetry once returned continues (Fig. S3). The return to

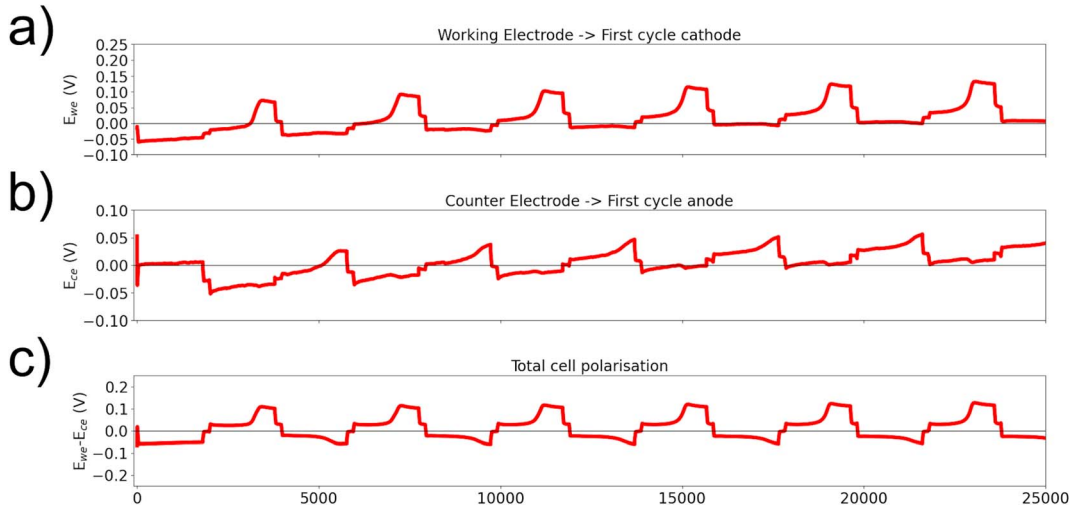

Fig. 6 Cycling of a 3-electrode Swagelok cell with Li_2Ca intermetallic as the working electrode, LREM as the counter electrode and Li metal as the reference electrode. Current cycled at 0.2 mA cm^{-2} for 1800 s with 180 s of rest in between alternating polarizations.

symmetry in both cases could be considered as a loss of the easy availability of the extra plated capacity either through consumption (SEI or "dead" lithium formation) or an indication that the lithium has been plated into the bulk and so cannot be distinguished from the pristine electrode behaviour.

2.2.2 Asymmetric electrodes. To explore the difference between surface plating and deposition on the eutectic structure, an LiTFSI 3-electrode Swagelok cell was fabricated with electrodes made of the LREM and a solid Li_2Ca intermetallic and using lithium metal as the reference electrode (Fig. 6). Here, the solid intermetallic can only have lithium plated onto the surface, and the LREM is now cycled between full and partially empty states. The intermetallic is labelled as the working electrode in Fig. 6 and is stripped during even half-

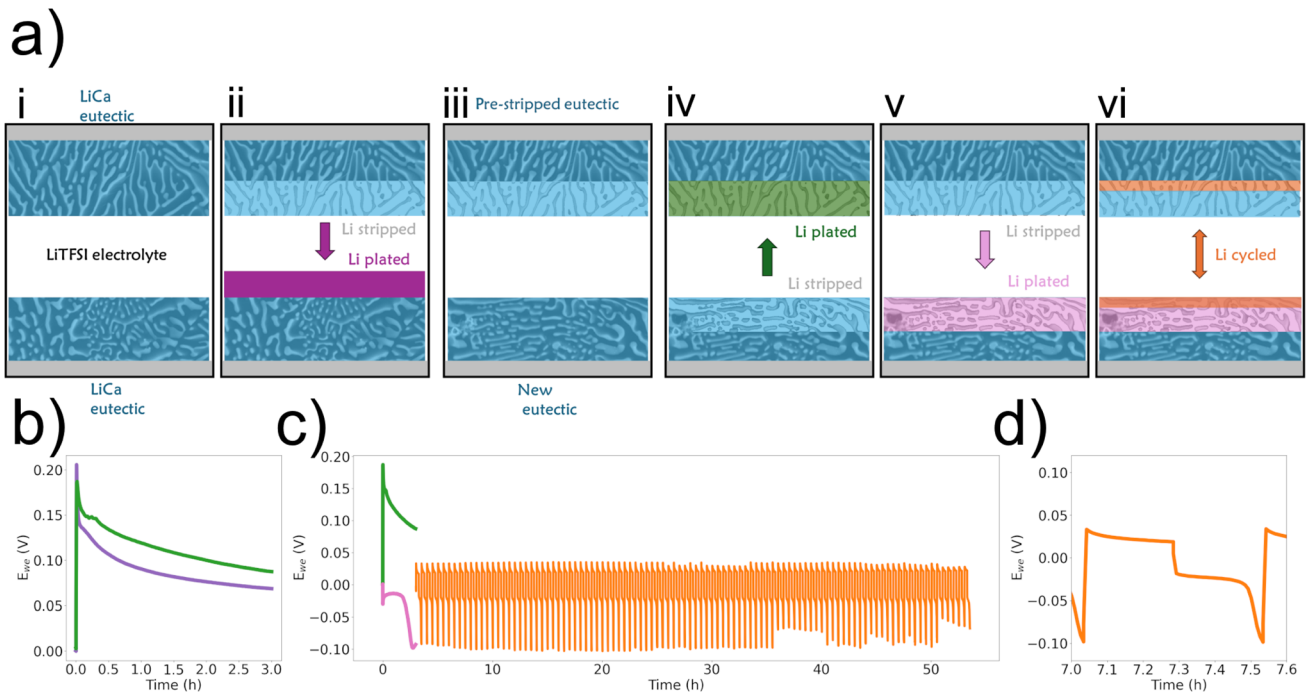

Fig. 7 (a) Schematic of the asymmetry cell formation and cycling: (i) starting cell, (ii) long strip half-cycle, (iii) new cell with a pre-stripped electrode, (iv) plating onto the stripped electrode, (v) reverse of the long half-cycle, and (vi) shorter cycling of the asymmetrically filled electrodes. The colours match the traces in (b–d), where purple, green, and pink denote the permanent movement of lithium and orange indicates the cycled lithium. (b) Deep stripping of an electrode shown in (ii) (purple) and re-plated/refilled electrode in a fresh cell shown in (iv) (green). (c) Same refilling data from (b) & (iv) shown with the reversed long half-cycle shown in (v) (pink) and then the cycling shown in (vi) (orange). (d) One typical full cycle of the asymmetrically filled cell.

cycles, and the LREM (counter electrode) is stripped during odd half-cycles. The total cell polarization is lower when the LREM is being stripped than when lithium is being taken from the surface of the intermetallic. This cell uses LiTFSI, and the initial cathode nucleation peak appears to be reduced compared to the symmetric case. The cathode nucleation peak for the intermetallic is lower than that for the LREM, suggesting that it is easier to deposit on the stripped eutectic surface. The secondary peak associated with a stripping process requiring a higher voltage is still visible when the intermetallic is acting as the anode but is significantly smaller for the LREM (maximum polarisation: intermetallic, 0.11 V; LREM, 0.05 V), leading to an asymmetry in the total cell polarisation. This suggests that the lower secondary peaks observed in LiTFSI symmetric cells are a result of the easy cyclability of lithium into and out of the eutectic structure, with the potential only increasing when extra lithium is being first extracted from deep in the 3D composite electrode.

To test the most extreme case with an LiTSFI electrolyte, an LREM electrode was stripped to remove 80% of the primary lithium metal, and then the cell was disassembled and the emptied electrode was put into a new cell (Fig. 7). A schematic is shown in Fig. 7a to describe the process: (i) starting with a symmetric cell, (ii) lithium is stripped from one electrode (purple), (iii) the stripped electrode is then moved to a new cell, (iv) where it is re-plated (green), (v) followed by another long half-cycle (pink), before (vi) cycling a small amount symmetrically (orange). This is to explore the difference between the first half-cycle of a symmetric cell where stripping is from the eutectic structure and plating on a pristine surface (purple line) to a cell where stripping occurs from the LREM and plating is done onto an emptied intermetallic 3D structure (green line) (Fig. 7b). The initial peak (cathode nucleation) is higher for the smooth surface (purple) than for the 3D intermetallic (green), but the potential is higher for the 3D intermetallic for the remainder of the half-cycle. This suggests that it is easier to nucleate new Li (or enter the intermetallic) for the 3D structure than on a Li_2Ca surface and that there is an additional resistance associated with plating onto the 3D structure over plating onto a surface. In both cases, the anode potential (stripping) should be the same as the electrode being stripped starts fresh/full. When this cell is cycled, there is an asymmetry in the half-cycle potentials due to the long initial cycle, as seen in Fig. 5a(v, vi) and c, meaning one electrode has more lithium easily accessible and the other adds lithium deeper at a potential cost each time. Therefore, no secondary peak is observed during stripping from the WE because the capacity being moved is a fraction of that moved during the initial plate and stripping, so the lithium availability is high (Fig. 5d). There is also an asymmetry in the primary peak; it is lower (~0.02 V) during the plating to the deep stripped and re-plated electrode (shown as

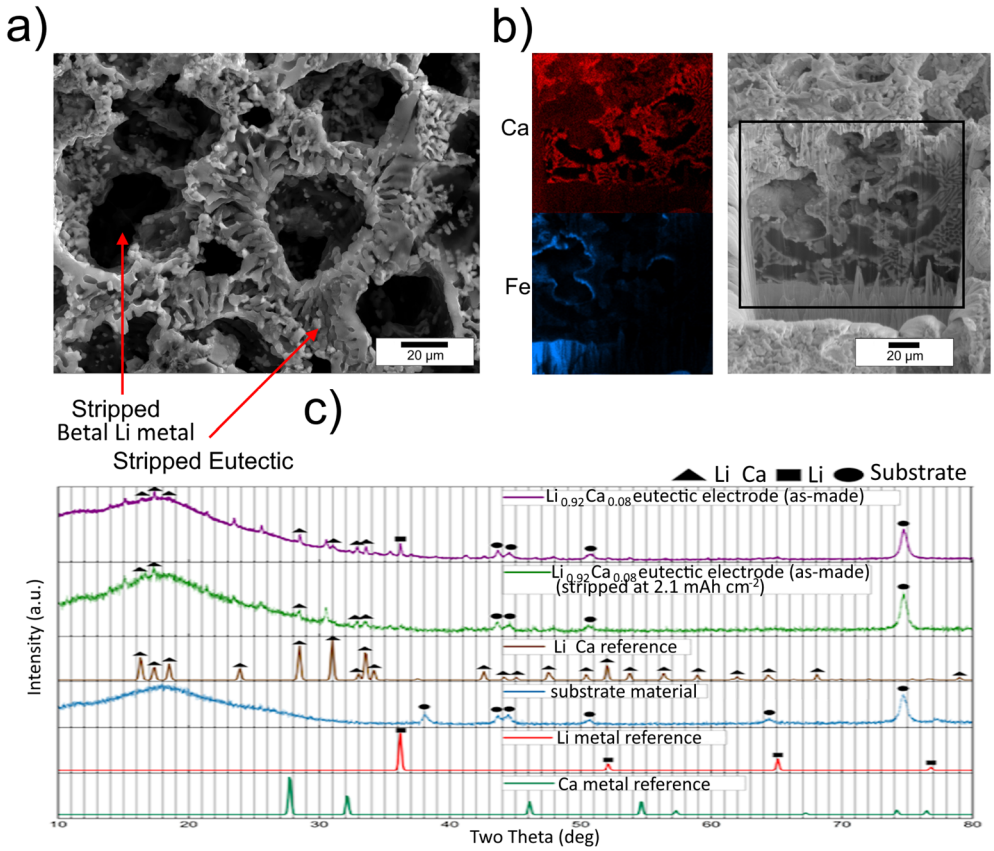

Fig. 8 (a) Secondary electron SEM image of the surface of a WE stripped of 38% of its lithium capacity. (b) FIB cross-section of a WE stripped of 53%, with EDX maps from the central region to highlight the Fe in the stainless steel current collector and the Ca rich intermetallic phase. (c) XRD data from as-formed and deep stripped electrodes with reference data for the expected phases.

the pink region in the schematic (vi) than to the emptier LREM that is deep stripped (~0.04 V).

2.3 Microstructural changes during cycling

Characterisation of the cycled electrodes can be used to understand the physical changes occurring in these experiments, especially those that lead to the alloy anode outperforming the lithium metal anode at current densities greater than 1 mA cm^{-2}. Fig. 8a shows the SEM image of the honeycomb structure remaining when an alloy anode has 38% of its theoretical capacity removed electrochemically from a symmetric cell using $LiPF_6$ as the electrolyte. During the 0.2 mA stripping for 15 hours, the pure lithium metal regions have been removed preferentially, suggesting, as expected, that they are energetically easier to strip than for lithium to be electrochemically extracted from the intermetallic phase. XRD analysis shows a significant reduction in the lithium metal peaks but did not detect any additional peaks associated with calcium metal upon stripping, which suggests that Li_2Ca in the electrode is stable upon lithium extraction to this capacity (Fig. 8c). FIB cross-sections show voids deep into the material where lithium metal has been removed, but not all of these are in direct contact with the electrolyte, highlighting that during electrochemical stripping there must have been a flow of lithium through the intermetallic phase (Fig. 8b). The EDX data for Fe show both the current collector at the bottom of the image and redeposited Fe (from the ion milling process) that highlights the edges of voids. A clear distinction between lithium metal (black) and the void (light red) can also be seen in the EDX data for Ca, as well as the bright red calcium rich phases. This electrode was stripped for 20 hours at 0.2 mA to remove 53% of its theoretical lithium capacity, suggesting that lithium is removed progressively through the electrode, with the lithium closest to the current collector (bottom of the image) being removed last.

Re-plating lithium (15 hours at 0.2 mA) into a stripped electrode (15 hours at 0.2 mA) using $LiPF_6$ as the electrolyte displays evidence of lithium dendrite formation (Fig. 9). This contrasts with the smooth and compact surface reported by Jia *et al.*[9] Fig. 9a shows that the 3D honeycomb eutectic structure remains visible, and PFIB cuts into the lithium formations on the surface reveal that they are not fully dense and that the depth of the voids in the electrode is smaller than that in the sample that was only stripped (Fig. 8 and 9b). Using PFIB to observe the subsurface microstructure of a region considered 'full dense' from the surface reveals a void at the interface between the electrode and the current collector, suggesting that lithium was removed from this region but not fully redeposited (Fig. 9b). Estimating the volume of surface deposits from SEM images of this kind, and assuming it is fully dense, suggests that a mass of 0.48 mg is plated onto the electrode surface significantly below the 0.78 mg of capacity theoretically plated. Given

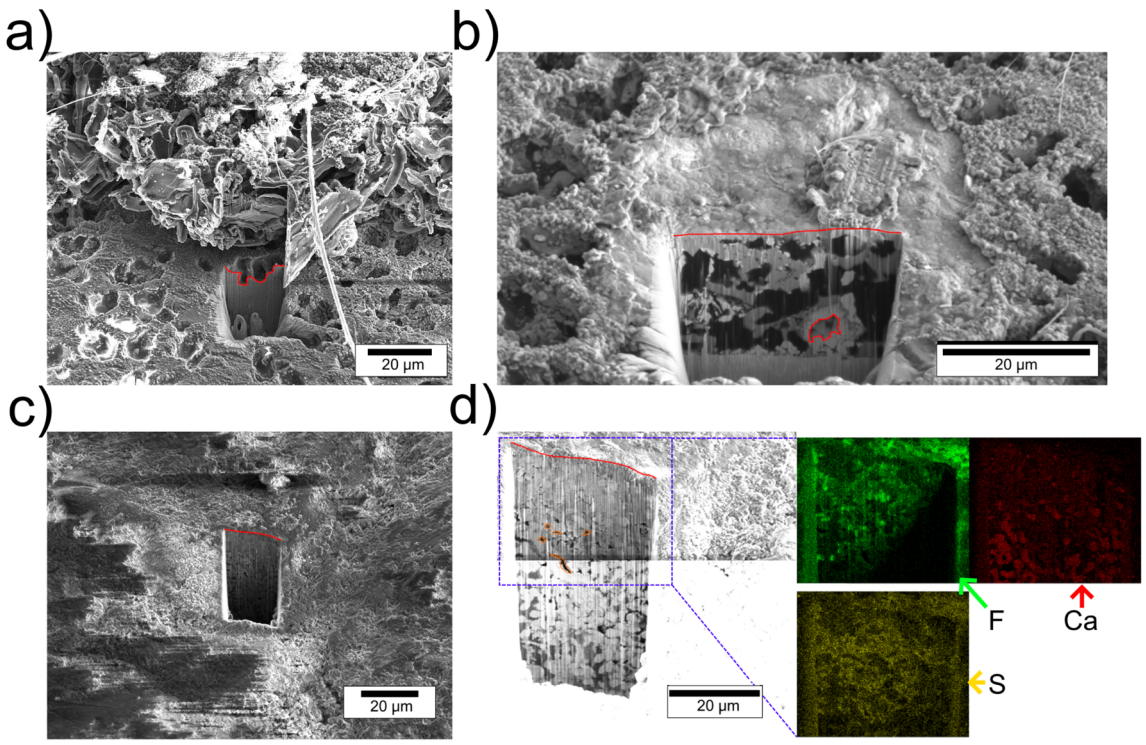

Fig. 9 (a) SEM image of the $LiPF_6$ stripped and re-plated electrode surface with a PFIB cut cross-section through a lithium surface deposit and (b) a cross-section through a region assumed to be 'fully dense' from the surface. (c) The surface of a cycled LiTFSI electrode with a cross-section through a re-plated 'fully dense' region. (d) A composite image of the cross-section (with varying contrast levels) to show the voids present and EDX maps from the region highlighted in blue showing the presence of electrolyte elements (F and S) deep into the electrode bulk. The red line shows the surface for each PFIB cut.

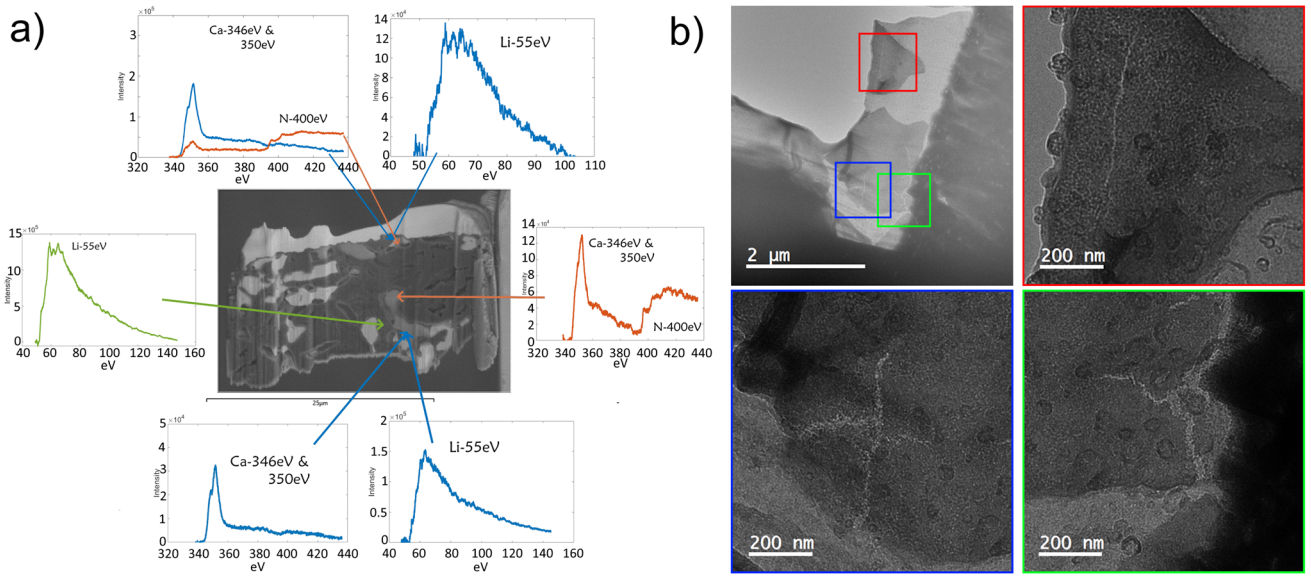

Fig. 10 (a) EELS spectra of selected spots in a sample to isolate different phases in a deep stripped and re-plated sample. Spectral colours denote the presence of metals as follows: green – only lithium, blue – lithium and calcium, and orange – only calcium. (b) TEM images showing cracks in the "intermetallic" (dark phase in the images).

that the FIB cross-sections highlight the lithium deposits on the surface are not fully dense, we can conclude that close to 40% of lithium transported to the electrode re-enters the 3D microstructure. By contrast, cells cycled with LiTFSI electrolyte do not display the surface depositions, and an electrode cycled for 1000 h as a symmetric cell is shown in Fig. 9c. Here, infiltration of F and S from the electrolyte gives an indication of the depth to which stripping has occurred and then lithium has been re-plated onto the structure, reproducing a smooth top surface to the electrode. Re-plating is not perfect as there remain a small number of voids that are ~ 1 micron in length, which are highlighted in orange in Fig. 9d. These can be distinguished from the lithium metal phase as the topological 'curtaining' effect from the PFIB cutting is lost in those small areas. The EDX map of Ca shows the intermetallic phase and indicates that the solid regions without Ca are re-plated lithium metal, Fig. 9d. The surface of the LiTFSI cycled sample is not uniform but did not display surface dendrites, which supports the theory that regions where lithium has been re-plated onto the intermetallic structure are easier to strip than the 'fresh' uncycled regions that are visible on the left hand side of Fig. 9c. The EDX results also indicate the penetration of S and F from the liquid electrolyte into the solid electrode, indicating the depth to which the original primary lithium metal is likely to have been stripped, allowing for the liquid to flow in.

Lifting out the region shown in Fig. 9b as a TEM lamella allows for characterization *via* electron energy loss spectroscopy. Fig. 10 shows EELS spectra of specific phases in the material. The green spectra denote lithium metal where no peaks were present in the 340–440 eV range that would indicate the presence of calcium or nitrogen. The blue spectra collected from the same point highlight the Li_2Ca intermetallic. The orange central spectra highlight a region where there is no lithium peak measurable, but there is a distinct calcium peak accompanied by a nitrogen peak. All materials are carefully handled in an argon glovebox throughout, and so the only place they would interact with nitrogen is in the PFIB or the TEM. It is standard for high vacuum systems (SEM, PFIB, and TEM) to use dry nitrogen as a vent gas for bringing samples back up to atmospheric pressure before removal. Therefore, during this work, as samples are moved between instruments, they will have been exposed to dry nitrogen. Previous studies have shown that the Li–Ca intermetallic does not react with nitrogen gas even at 500 °C.[19] This suggests the presence of calcium metal that reacts when exposed to nitrogen, and not the intermetallic. This implies that lithium can leave the intermetallic during stripping and that it can plate lithium metal into the porous 3D structure without reforming all of the intermetallic electrochemically.

TEM of a foil extracted from the same sample in a non-"fully dense" region provides further evidence that lithium has been removed from the intermetallic (presumably after it was first stripped from the primary lithium regions) and then on re-plating it has not returned. Fig. 10b shows that the removal of material by delithiation of the intermetallic regions results in cracks forming due to an increase in the density during transformation from Li_2Ca (1.08 g cm^{-2}) to Ca (1.53 g cm^{-2}).[20,21]

3 Discussion

The results shown here illustrate that characterisation using electron microscopy and plasma FIB sectioning can help understand the electrochemical processes during cell cycling. Interpretation without EM of the data observed for the cycling of the LREM electrodes suggests that lithium is only cycled from the surface, but subsurface cross sections in Fig. 9 highlight

that there is redeposition into the 3D intermetallic scaffold. The electrochemical data however highlight that cycled lithium is more accessible (requires a lower potential) than 'fresh' lithium from deeper in the structure, but crucially the stable interface between the intermetallic and the electrolyte allows this to happen at a lower potential than with a lithium only anode, even at higher current densities. This lower potential could also reduce the formation of side products during high current density cycling. The role of the electrolyte is observed to be similar to the lithium metal anode case, whereby more dendritic growth is seen with $LiPF_6$, but this does not stop lithium from being re-plated onto the 3D structure. The effect of different nucleation potentials versus growth/insertion of lithium was not observed, and more prominent was the reduced cathode potential for lithium entering a pre-stripped electrode than nucleating onto a surface. The elevated long plate potential (Fig. 5b) suggests that plating onto the eutectic structure is slower than the growth of lithium dendrites but easier than surface nucleation, effectively providing a local energy minima that prioritises re-filling over dendrite nucleation at an elevated potential relative to symmetric Li metal cells. The slower kinetics for plating onto the eutectic structure is supported by an estimation of the diffusion coefficient for Li in Li_2Ca at room temperature as $\sim 9^{-12}$ cm^2 s^{-1} (Fig. S7). This value is significantly below the expected diffusion coefficient in lithium (10^{-10}) and estimates for other lithium intermetallic systems.[22] Asymmetric cycling also highlighted the benefit of pre-emptying and refilling to remove the high secondary peak potential associated with the anodic dissolution reaction of stripping lithium from the electrode. The presence of the secondary "anode" peak in all half-cycles where no large excess of re-plated lithium is present suggests that even with LiTFSI there is some loss of capacity requiring 'fresh' lithium to be extracted from the eutectic structure at the end of each half-cycle. In the increasing cycle time example with $LiPF_6$, this can be seen as almost 30% of the capacity consistently, and with LiTFSI the plateau is closer to 8% of the cycled capacity. In either case, this suggests a potential issue for cycling the thinner electrodes required for high energy density cells. To highlight this, a symmetric cell produced with 20 μm thick electrodes was cycled at 1.1 mA cm^{-2} using a cycling capacity of 0.53 mA h cm^{-2} in an $LiPF_6$ electrolyte and failed after only 30 cycles. Assuming this failure is the result of exhausting the capacity through the 30% loss per cycle observed above equates to $\sim$10 mA h cm^{-2} which is close to the theoretically available lithium (8.5 mA h cm^{-2}) if only the lithium in the primary metal phase is electrochemically active. The observations by TEM and STEM suggest that the intermetallic can be stripped to form calcium metal and that this does not appear to effect the cycling of the region but may effectively contribute some additional capacity. Cycling data from cells that have had a large capacity stripped from them can be seen in Fig. S5 and show, as expected, that the potential observed is dependent on the current used to extract lithium from the electrode and the proportion of lithium metal available. As the lithium metal store is decreased, it is taken from deeper and deeper within the 3D eutectic, leading to a higher potential. This potential could be enough in places to delithiate the intermetallic, but there is no indication that this happens at lower potentials or lower levels of discharge. Jia *et al.* showed XRD on bulk samples that the lithium metal peaks are lost first on delithiation, around 75% of the theoretical capacity, at a potential of 0.11 V *vs.* Li/Li^+ with a current of 0.5 mA cm^{-2}, which agree with our data (Fig. S4). Upon delithiation to 100% theoretical capacity, Jia *et al.* observed a loss of Li_2Ca peaks and the appearance of Ca metal peaks. Relithiating this Ca foam, the reverse is seen (loss of Ca metal peaks and appearance of Li_2Ca peaks) before Li metal peaks appear. They show no difference in the potential for these two processes and suggests that a large amount of the Ca can be relithiated, but our local TEM observation illustrates that no complete perfect conversion happens throughout the anode. This potentially consumes the intermetallic, but the Ca metal remains electrochemically active.

4 Conclusions

This paper shows how lithium leaves and re-enters a 3D electrode that is made *via* simple alloying and liquid casing at low temperatures. The role of electrolyte in the LREM alloy anode cycling was explored. Lithium metal is shown to be stripped from the electrode down to the current collector, while the surface of the electrode is maintained by calcium intermetallic, preserving the exterior physical structure. The system behaves when lithium is stripped out, but if too much is removed then the intermetallic is lost leaving calcium metal that can become chemically reactive if exposed. Re-plating lithium metal onto the 3D structure is successful, but there is no indication that lost intermetallic is regained.

5 Experimental details

5.1 Fabrication of electrodes

Li sheets (99%, Sigma-Aldrich) and Ca metal lumps (99%, Goodfellow) were used. Li and Ca were weighed out and cast on a hotplate (Stuart) in an argon glovebox (MBraun) with a controlled atmosphere of <5 ppm O_2 and H_2O. The alloys were cast at temperatures >230 °C, above the melting point of the intermetallic phase. While molten, the alloys were made into small pellets by scooping the molten alloy with a spatula and letting it solidify before immediately breaking it into lumps. These were weighed out into masses of $\sim$3 mg and cast onto current collectors at 250 °C. Current collectors used were stainless steel discs (diameter: 15.5 mm × T0.2 mm, Pi-KEM). Spatulas were used to aid the spreading of the material across the current collector surface. The thickness of electrodes made with this method was approximately 20 μm. To cast the pristine lithium electrodes, lithium was cast directly onto the current collectors.

5.2 Cell assembly

The fabricated Li–Ca lithium-rich eutectic microstructure (LREM) electrode and pristine lithium electrode (8 mm diameter) were assembled into symmetric coin cells of CR2032 type using standard stainless steel cell components. GF/F glass fibre discs were used as the separator material, wetted separately

with 75 μL of liquid electrolytes, $LiPF_6$ (electrolyte composed of 1.0 M lithium hexafluorophosphate in ethylene carbonate/dimethyl carbonate (50/50, v/v), Sigma Aldrich)) and LiTFSI (1 M lithium bis(trifluoromethanesulfonyl)imide in 1,2-dimethoxyethane and 1,3-dioxolane (50/50, v/v) with 2% $LiNO_3$ (Col-Int Tech, USA)). A three-electrode Swagelok cell with LiTFSI electrolyte was also made with Li–Ca eutectic working and counter electrodes and a lithium metal reference electrode. All the cells were kept for achieving stabilization over a period of 12 hours before electrochemical analysis.

5.3 Microstructure and XRD characterisation

SEM was conducted using a Tescan Mira 3 FEG-SEM equipped with an energy-dispersive X-ray (EDX) spectrometer and a glovebox attachment to allow sample transfer in an inert environment. PFIB was used to section out regions of interest in the electrode structure. The instrument used was a Thermo Fisher Helios G4 PFIB CXe, and milling was conducted at cryogenic temperatures of −130 °C as there were issues with lithium contaminating the ion gun at ambient temperature. XRD was carried out on samples using a 3 kW Rigaku SmartLab X-ray diffractometer. Due to the air-sensitive nature of the samples, they were sealed with Kapton polyimide tape after being loaded onto a glass slide. This introduced a large background into the observed spectra in the low 2θ range. The background was not removed from the XRD plots to preserve as much data as possible. Measurements were recorded at a scan speed of $2^\circ\ min^{-1}$ over a 2θ range of 10–90°.

Author contributions

Conceptualization – C. G., P. D. N., Z. H., M. N., and D. E. J. A.; methodology – E. D. and S. O. V.; cell fabrication – S. O. V., Z. H. and M. N.; electrochemical data collection – S. O. V., Z. H. and M. N.; electron microscopy data collection – E. D.; software code – E. D.; validation – E. D.; formal analysis – E.D.; investigation – E. D.; data curation – E. D.; writing: original draft preparation – E. D.; writing: review & editing – E. D., J. A., S. O. V., C. G., D. E. J. A. and P. D. N.; visualizations – E. D.; supervision – E. D., S. O. V., and D. E. J. A.; project administration – E. D. and D. E. J. A.; funding acquisition – C. G., P. D. N., and D. E. J. A.

Conflicts of interest

There are no conflicts to declare.

Data availability

Data will be made available on the Oxford University Research Archive shortly after the paper has been published.

Supplementary information (SI) is available. See DOI: https://doi.org/10.1039/d5ta09847e.

Acknowledgements

This research was funded in whole, or in part, by the UKRI Faraday Institution [SOLBAT FIRG026 and FIRG056]. For the purpose of Open Access, the author has applied a CC BY public copyright licence to any Author Accepted Manuscript version arising from this submission. The authors acknowledge the use of characterisation facilities within the David Cockayne Centre for Electron Microscopy, Department of Materials, University of Oxford, alongside financial support provided by the Henry Royce Institute (Grant ref EP/R010145/1).

References

1 V. Viswanathan, A. H. Epstein, Y. M. Chiang, E. Takeuchi, M. Bradley, J. Langford and M. Winter, *Nature*, 2022, **601**, 519–525.
2 D. Lin, Y. Liu and Y. Cui, *Nat. Nanotechnol.*, 2017, **12**, 194–206.
3 K. G. Gallagher, S. Goebel, T. Greszler, M. Mathias, W. Oelerich, D. Eroglu and V. Srinivasan, *Energy Environ. Sci.*, 2014, **7**, 1555–1563.
4 G. Bieker, M. Winter and P. Bieker, *Phys. Chem. Chem. Phys.*, 2015, **17**, 8670–8679.
5 D. Aurbach, *J. Power Sources*, 2000, **89**, 206–218.
6 C. P. Yang, Y. X. Yin, S. F. Zhang, N. W. Li and Y. G. Guo, *Nat. Commun.*, 2015, **61**(6), 1–9.
7 J. Xiang, L. Yuan, Y. Shen, Z. Cheng, K. Yuan, Z. Guo, Y. Zhang, X. Chen and Y. Huang, *Adv. Energy Mater.*, 2018, **8**, 1802352.
8 W. Jia, T. Chen, Y. Wang, S. Qu, Z. Yao, Y. Liu, Y. Yin, W. Zou, F. Zhou and J. Li, *Electrochim. Acta*, 2019, **309**, 460–468.
9 W. Jia, Z. Wang, J. Li, X. Yu, Y. Wei, Z. Yao, Y. Liu, Y. Wang, A. Zhou, W. Zou, F. Zhou and H. Li, *J. Mater. Chem. A*, 2019, **7**, 22377–22384.
10 Y. Xu, H. Wu, Y. He, Q. Chen, J. G. Zhang, W. Xu and C. Wang, *Nano Lett.*, 2020, **20**, 418–425.
11 C. W. Bale and A. D. Pelton, *J. Phase Equilib.*, 1987, **8**, 125–127.
12 D. Fauteux and R. Koksbang, *J. Appl. Electrochem.*, 1993, **23**, 1–10.
13 M. Debessai, T. Matsuoka, J. J. Hamlin, A. K. Gangopadhyay, J. S. Schilling, K. Shimizu and Y. Ohishi, *Phys. Rev. B:Condens. Matter Mater. Phys.*, 2008, **78**, 214517.
14 Y. Wang, Y. Liu, M. Nguyen, J. Cho, N. Katyal, B. S. Vishnugopi, H. Hao, R. Fang, N. Wu, P. Liu, P. P. Mukherjee, J. Nanda, G. Henkelman, J. Watt, D. Mitlin, Y. Wang, Y. Liu, H. Hao, R. Fang, N. Wu, P. Liu, D. Mitlin, M. Nguyen, J. Cho, N. Katyal, G. Henkelman, B. S. Vishnugopi, P. P. Mukherjee, J. Nanda and J. Watt, *Adv. Mater.*, 2023, **35**, 2206762.
15 J. Qian, W. A. Henderson, W. Xu, P. Bhattacharya, M. Engelhard, O. Borodin and J. G. Zhang, *Nat. Commun.*, 2015, **61**(6), 6362.
16 R. F. Egerton, *Phys. Princ. Electron Microsc. An Introd. to TEM, SEM, AEM*, 2nd edn, 2016, pp. 1–196.
17 K. N. Wood, E. Kazyak, A. F. Chadwick, K. H. Chen, J. G. Zhang, K. Thornton and N. P. Dasgupta, *ACS Cent. Sci.*, 2016, **2**, 790–801.
18 K.-H. Chen, K. N. Wood, E. Kazyak, W. S. LePage, A. L. Davis, A. J. Sanchez and N. P. Dasgupta, *J. Mater. Chem. A*, 2017, **5**, 11671–11681.

19 W. X. Yuan, J. Li, G. Wang, A. G. Cheng and X. Zhao, *J. Cryst. Growth*, 2006, **290**, 621–625.
20 K. Persson, *Materials Data on Li2Ca (SG:194) by Materials Project*, 2016.
21 J. W. Arblaster, *Selected Values of the Crystallographic Properties of Elements*, ASM International, 2018.
22 M. Pasta, J. Aspinall and F. Shen, *et al.*, High Diffusivity Lithium Intermetallic in Two-Phase Alloy Negative Electrode for Solid-State Batteries, *Research Square*, 2025, Preprint (Version 1), DOI: 10.21203/rs.3.rs-6759455/v1.